Suppressed recombination loss in organic photovoltaics adopting a planar–mixed heterojunction architecture

Kui Jiang [1,2,3,13], Jie Zhang [4,13], Cheng Zhong [5,13], Francis R. Lin [1,2,3] ✉,
Feng Qi [2,3], Qian Li [6], Zhengxing Peng [7], Werner Kaminsky [8], Sei-Hum Jang [9],
Jianwei Yu [10], Xiang Deng [1,3], Huawei Hu [11], Dong Shen [2], Feng Gao [10],
Harald Ade [7], Min Xiao [6], Chunfeng Zhang [6,12] ✉ & Alex K.-Y. Jen [1,2,3,9] ✉

At present, high-performance organic photovoltaics mostly adopt a bulk-heterojunction architecture, in which exciton dissociation is facilitated by charge-transfer states formed at numerous donor–acceptor (D-A) heterojunctions. However, the spin character of charge-transfer states originated from recombination of photocarriers allows relaxation to the lowest-energy triplet exciton (T_1) at these heterojunctions, causing photocurrent loss. Here we find that this loss pathway can be alleviated in sequentially processed planar–mixed heterojunction (PMHJ) devices, employing donor and acceptor with intrinsically weaker exciton binding strengths. The reduced D-A intermixing in PMHJ alleviates non-geminate recombination at D-A contacts, limiting the chance of relaxation, thus suppressing T_1 formation without sacrificing exciton dissociation efficiency. This resulted in devices with high power conversion efficiencies of >19%. We elucidate the working mechanisms for PMHJs and discuss the implications for material design, device engineering and photophysics, thus providing a comprehensive grounding for future organic photovoltaics to reach their full promise.

Organic photovoltaics (OPVs) are promising for clean energy because of their vast molecular tunability in photoactive materials[1–3]. The proof-of-concept OPV absorber demonstrated in the 1980s adopted a sequentially vacuum-deposited bilayer architecture[4]. This showed very low efficiency, reflecting the limited material properties and processing techniques. Until 1995, bulk-heterojunction (BHJ) architecture comprising a highly intermixed donor:acceptor (D:A) network was found to greatly improve cell performance by facilitating exciton dissociation

[1]Department of Materials Science and Engineering, City University of Hong Kong, Kowloon, Hong Kong. [2]Department of Chemistry, City University of Hong Kong, Kowloon, Hong Kong. [3]Hong Kong Institute for Clean Energy (HKICE), City University of Hong Kong, Kowloon, Hong Kong. [4]Center for Photonics Information and Energy Materials, Shenzhen Institute of Advanced Technology, Chinese Academy of Sciences, Shenzhen, Guangdong, PR China. [5]Department of Chemistry, Wuhan University, Wuhan, Hubei, PR China. [6]National Laboratory of Solid State Microstructures, School of Physics, and Collaborative Innovation Center for Advanced Microstructures, Nanjing University, Nanjing, Jiangsu, PR China. [7]Department of Physics and Organic and Carbon Electronics Laboratories (ORaCEL), North Carolina State University, Raleigh, NC, USA. [8]Department of Chemistry, University of Washington, Seattle, WA, USA. [9]Department of Materials Science and Engineering, University of Washington, Seattle, WA, USA. [10]Department of Physics Chemistry and Biology (IFM), Linköping University, Linköping, Sweden. [11]College of Materials Science and Engineering, Donghua University, Shanghai, PR China. [12]Institute of Materials Engineering, Nanjing University, Nantong, Jiangsu, PR China. [13]These authors contributed equally: Kui Jiang, Jie Zhang, Cheng Zhong. ✉e-mail: franclin@cityu.edu.hk; cfzhang@nju.edu.cn; alexjen@cityu.edu.hk

in OPV absorbers[5]. The nanoscale phase-separated domains and energy offsets at numerous D-A heterojunctions help overcome the short diffusion lengths[1,6,7] and large exciton binding energy[1,8,9] in organics. Based on this concept, vibrant research has led to the development of very efficient pseudo-2D non-fullerene acceptors (NFAs) represented by BTP-4F (Y6)[2]. They possess strong near-infrared (NIR) photoresponse in conjunction with low interfacial energetic disorder due to enhanced intermolecular π−π interactions and unique solid-state packing patterns[10,11]. Power conversion efficiencies (PCEs) of greater than 18% have been reported[12], representing the state of the art.

However, it is a major challenge to continuously improve OPV performance to reach theoretically achievable values. In a BHJ, charge-transfer (CT) states with both singlet ([1]CT) and triplet ([3]CT) spin characters ([1]CT/[3]CT) can be formed at numerous D-A heterojunctions through non-geminate recombination of free charges[13] dissociated from photoexcited local excitons (LE) with mediation of [1]CT (Fig. 1a). The relaxation of CT states dominates the energy loss in OPV, undermining the short-circuit current density (J_{SC})[14]. To prevent such cascade relaxation processes, strategies have been applied to minimize the spin-mediated relaxation between [3]CT and the lowest-energy triplet exciton (T_1), including promoting wavefunction delocalization[13] and molecular engineering of the T_1 energy level[15–17] in both fullerene and non-fullerene OPVs. Nevertheless, the role of these densely populated interfacial CT states in BHJ is an intermediate between excitons and free carriers. The [1]CT formed prior to the charge-separated (CS) state facilitates exciton dissociation and thus free carrier formation (LE→[1]CT→CS), but the [1]CT/[3]CT from non-geminate recombination tend to relax to ground state if insufficient repopulation to CS state occurs, inevitably causing photocurrent loss.

Intriguingly, spontaneous formation of intermolecular delocalized singlet excitons (DSE) in neat pseudo-2D NFAs under condensed phase was observed upon photoexcitation[18], which was also identified to be capable of mediating the pathway of free carrier formation in the OPV blend (LE→DSE→CS). Such a pathway is indicative of the weaker dependency of [1]CT for exciton dissociation in these materials, which creates hope that the CT-mediated loss pathways can be mitigated. In this vein, we have discovered that sequentially deposited donor/acceptor (D/A) PMHJ OPVs employing materials with intrinsically weaker exciton binding strengths are capable of hindering CT-mediated loss pathways. The fewer D-A contacts in PMHJ suppress the formation of recombined CT states and result in reduced T_1 concentration, as spectroscopically evidenced in this study. Single-junction OPVs with high PCEs surpassing 19% were subsequently achieved based on our findings.

PMHJ as an effective strategy to realize efficient OPVs

Sequentially processed OPVs have shown potential to compete with or even outperform one-step processed BHJ cells in recent studies[7,19–21], however, the reason behind these observations is yet unclear. Unlike conventional BHJs processed from a pre-mixed D:A solution, our PMHJ is processed in a two-step manner by spin-casting the chloroform solution of NFA on top of the thin-film of donor polymer PDTBT2T-FTBDT (D18). D18 exhibits strong temperature-dependent aggregation properties and limited solubility, and is pre-deposited from its solution in hot chlorobenzene[22] (Supplementary Fig. 4). Without further post-treatments and additives, a rather de-mixed blend with reduced D-A heterojunctions and non-uniform out-of-plane material distribution can be achieved (Fig. 1e). The obtained high PCEs of 18.22% (D18/T9TBO-F) and 18.30% (D18/T9SBN-F) (Fig. 1b–d) indicate extremely efficient photo-to-current conversion with minimized photovoltage–photocurrent trade-offs in binary PMHJ cells (Fig. 2a and Supplementary Table 2). The open-circuit voltage (V_{OC}) and non-radiative V_{OC} loss (Supplementary Figs. 19, 20 and Supplementary Table 12) are comparable to those reported for high-performance devices[23–25]. This method also shows satisfactory reproducibility (Supplementary Fig. 6), which

is critical for OPV practical applications, especially while D18 is very difficult to process in BHJ form due to its hard-to-control strong aggregation[22]. For comparison, BHJ cells with identical material systems were also fabricated and showed lower PCEs of 17.21% (D18:T9TBO-F) and 17.07% (D18:T9SBN-F) (Supplementary Fig. 5 and Supplementary Table 2), due to their lower fill factors (FFs) from less balanced charge-carrier mobilities in BHJ blends (Supplementary Fig. 10 and Supplementary Table 4)[26], and more importantly, their inferior J_{SC} values.

The scope of this study was further broadened by conducting a comprehensive mapping of material systems covering 14 NFAs in the D18/NFA PMHJ device form to prove the general applicability of this approach, including Y6, T9TBO-F, T9SBN-F and, additionally, 11 NIR-absorbing NFAs[11,27,28] (Supplementary Figs. 1–3), which showed high PCEs ranging from 17.53 to 18.30% (Supplementary Fig. 5 and Supplementary Table 3). The ternary strategy was applied to successfully improve the V_{OC} of PMHJ cells (Supplementary Table 3). By adding a medium bandgap NFA Y6-O (ref. [29]) in the NFA precursor solution then spin-cast over pre-deposited D18 thin-film, it gave a ternary PMHJ to achieve high PCEs of over 19% in the single-junction devices of D18/T9TBO-F:Y6-O (Fig. 2a) and extensively NIR-absorbing D18/S9SBO-F:Y6-O (Supplementary Fig. 5 and Supplementary Tables 3). Devices employing D18/T9TBO-F:Y6-O and D18/S9SBO-F:Y6-O PMHJ have been certified by various authorities, one of which was the National Renewable Energy Laboratory in September 2020 (Supplementary Figs. 7–9).

Reducing exciton binding strength benefits PMHJ cells

To reveal the underlying mechanisms behind the high efficiency of PMHJ cells, comprehensive characterizations were performed on neat films of D18 and two NFAs, T9TBO-F and T9SBN-F, as well as their BHJ and PMHJ blends, to provide better understanding of their photophysical and morphological properties. The dynamics of excitons and photocarriers in materials were probed by transient absorption (TA) spectroscopy. Within -10 ps time scale, the Frenkel-type LE states (1,180 nm in neat D18; 915 and 930 nm in neat T9TBO-F and T9SBN-F, respectively, and their corresponding blends) emerge, of which the decay followed by uprising excited-state absorption (ESA) bands (940 nm in neat D18; 1,550 and 1,600 nm in neat T9TBO-F and T9SBN-F, respectively, and their corresponding blends) indicating fast conversion (<1 ps) of LE into an intermediate state (Fig. 3a–c and Supplementary Figs. 30–32). These ESA bands may correspond to an intermolecular DSE state (Supplementary Figs. 33, 42), where closely packed molecules help reduce exciton binding energy and facilitate the formation of excited species with CT characters[10,18].

The packing of materials was then simulated by molecular dynamics (MD) calculations to investigate the intermolecular interactions of the materials in condensed phase, coupling with density functional theory calculations to provide information from both structural and energetic aspects. The calculations revealed that the formation of DSE state with lower energy versus LE (Fig. 1a, Supplementary Figs. 21, 22 and Supplementary Tables 13–19) is facilitated by intimate packing of strongly interacting molecular moieties, dithienobenzothiadiazole in D18 and indanone in NFAs (Fig. 3d–f), respectively. The close packing of materials was also confirmed by X-ray crystallography of NFA single crystals, which consistently show intense J-aggregation-like packing patterns (Supplementary Figs. 12–14 and Supplementary Tables 5–8), and the grazing-incidence wide-angle X-ray scattering (GIWAXS) patterns of neat films and PMHJ blends (Supplementary Figs. 15–17, Supplementary Tables 9, 10 and Supplementary Notes III, IV). Besides facilitating the formation of DSE state with CT characters to aid exciton dissociation, intimate molecular packing of the materials may also promote exciton diffusion in D18 (ref. [30]) and NFAs. We have further confirmed the long exciton diffusion length in T9TBO-F (34 nm) from fluence-dependent TA dynamics measurements (Supplementary Fig. 46), which correlates
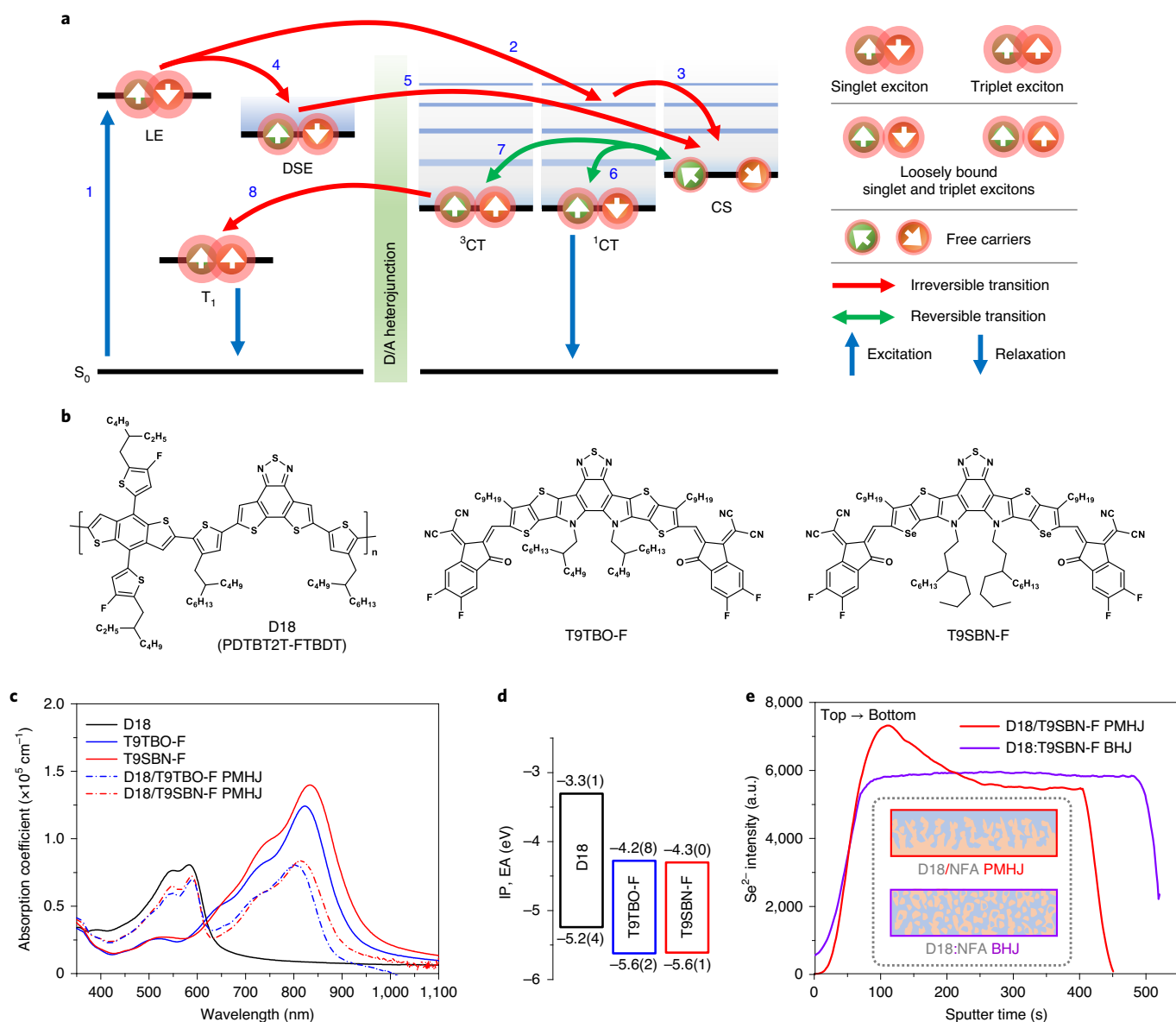
Fig. 1 | The Jablonski diagram and the active materials used for OPV fabrication. a, Illustration of excited-state dynamics in OPV: (1) photoexcitation of singlet excitons: $S_0{\rightarrow}LE$; (2, 4) transfer pathways of photoexcited singlet excitons: $LE{\rightarrow}{}^1CT$ (2) and $LE{\rightarrow}DSE$ (4); (3, 5) dissociation of loosely bound singlet excitons into free charges: $^1CT{\rightarrow}CS$ (3) or $DSE{\rightarrow}CS$ (5); (6, 7) CT states formation through non-geminate recombination: $CS{\rightarrow}{}^1CT/{}^3CT$, possibly with $^1CT/{}^3CT{\rightarrow}CS$ repopulation and spin-allowed $^1CT{\rightarrow}S_0$ relaxation; (8) $^3CT{\rightarrow}T_1$ relaxation, where further $T_1{\rightarrow}S_0$ relaxation can happen via triplet-charge annihilation, leading to permanent loss of photocarriers. **b,** Molecular structures of D18 and two major NFAs used in this study. **c,** Thin-film optical absorption of D18, NFAs and D18/NFA PMHJ blends. **d,** Energy level diagram of materials (IP: ionization potential corresponding to the highest occupied molecular orbital energy level; EA: electron affinity corresponding to the lowest unoccupied molecular orbital energy level.). **e,** ToF-SIMS Se^{2-} ion yield of D18/T9SBN-F PMHJ and D18:T9SBN-F BHJ blends plotted over sputtering time. The inset shows the schematic illustration of PMHJ and BHJ blends.

well with the square root of calculated Marcus rate (3.29×10^6 s$^{-1/2}$) reported in the literature[31].

In the PMHJ blends of D18/T9TBO-F and D18/T9SBN-F, the ESA bands representing the fast $LE{\rightarrow}DSE$ conversion within 0.1 ps were observed in NFA domains (Fig. 4a,e, Supplementary Figs. 39a–d, 40a–d). Later, within the time scale of 1–100 ps, polaron formation is indicated by the ESA band of CS states (765 and 790 nm in the corresponding blends of T9TBO-F and T9SBN-F, respectively) as confirmed by the photo-induced absorption measurements (Supplementary Fig. 42), followed by the decay of DSE signal, indicating the hole-transfer processes in the blends follow the pathway of $LE{\rightarrow}DSE{\rightarrow}CS$ that is consistent with the previously findings in the blends consisting of Y6[18]. The rigid molecular backbone and intimate packing of materials facilitate the formation of DSE state which synergistically decreases the dependency of exciton dissociation on CT states, ensuring efficient exciton transport in the PMHJ blends with lower degree of D-A intermixing[6,31]. Therefore, the criteria to realize efficient PMHJ cells can be fulfilled when both donor and acceptor materials employed have intrinsically weaker exciton binding strengths. This helps reduce the need for large amounts of D-A heterojunctions in BHJ to facilitate exciton dissociation and allow efficient generation of free carriers in PMHJ cells.

PMHJ outperforms BHJ by suppressing recombination loss

For a good absorber in OPVs, the efficiency of carrier generation should be maximized while that of carrier recombination ought to
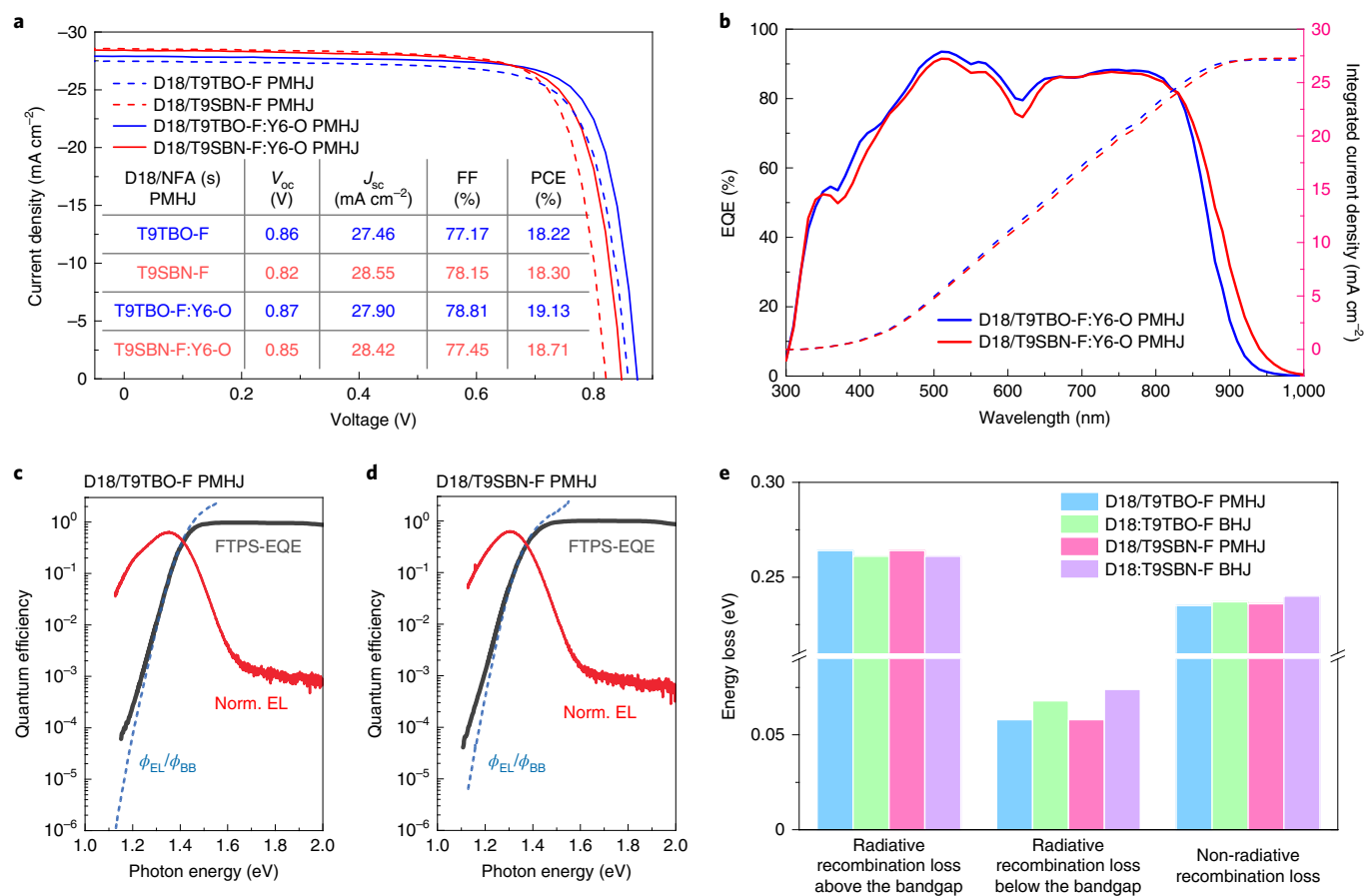
Fig. 2 | Photovoltaic cells characterizations. a, *J–V* characteristics of the best-performing PMHJ cells of binary D18/NFA (dashed lines) and ternary D18/NFA:Y6-O (solid lines). **b**, External quantum efficiency (EQE) spectra (solid lines) and integrated current densities (dashed lines) of the optimized cells. **c,d**, Semi-logarithmic plots of the normalized Fourier transform photocurrent spectroscopy-EQE (FTPS-EQE, grey line) and electroluminescence (red line) profiles of D18/T9TBO-F (**c**) and D18/T9SBN-F (**d**) cells plotted as a function of energy. The low-energy tailing of FTPS-EQE is theoretically proportional to the ratio of electroluminescence flux (ϕ_{EL}) and blackbody radiation spectrum (ϕ_{BB}, at 300 K), as indicated by the dark blue dashed line[49,50].

be minimized. While exciton dissociation in the PMHJ architecture has been proven to be efficient, we further discovered that PMHJs can also help to suppress recombination loss. In the PMHJ blends of D18/T9TBO-F and D18/T9SBN-F, an emerging ESA band at -1,440 nm was observed within the time scale of 100–1,000 ps, which is consistent with the spectral feature of T_1 in NFAs (Supplementary Figs. 34–37) as identified by triplet sensitization, indicating T_1 formation in the blends. In terms of time scale, T_1 in PMHJ blends forms closely behind the population of CS states, indicating a relaxation pathway originated from non-geminate charge recombination mediated by interfacial ^{3}CT. Changing the excitation fluence in TA experiments further showed that the relative signal intensity and the generation dynamics of T_1 are fluence-dependent, consolidating that T_1 originates from non-geminate recombination in the blends (Supplementary Fig. 38).

Interestingly, the ESA band representing T_1 formation was also observed in neat T9SBN-F film, accompanying with the decay of DSE state within the time scale of 1–500 ps (Fig. 3c and Supplementary Fig. 32). This could be due to efficient intersystem crossing between optically excited singlet excitons and T_1 due to heavy-atom effect brought by introducing selenium atom[15,32]. However, this does not affect the capability of sequentially processed D18/T9SBN-F PMHJ to suppress T_1 formation compared to its BHJ counterpart (Fig. 4e,f). On the other hand, although the pathways of exciton dissociation are still dominated by DSE state, the ESA bands of ground-state bleaching (GSB) and CS states emerge much less pronouncedly in the BHJ blends of D18:T9TBO-F and D18:T9SBN-F (Fig. 4b,f, Supplementary

Figs. 39e–h, 40e–h). Moreover, the T_1 ESA band appears significantly over time (10–500 ps), indicating the densely formed T_1 is relaxed from recombined ^{3}CT, leading to irreversible photocarrier loss. These results suggest that the PMHJ architecture is capable of suppressing T_1 formation (Fig. 4c,d,g,h), which is a unique example of demonstrating efficient T_1 suppression in non-fullerene OPVs through the carefully engineered active layer architecture using identical material systems. A similar trend of T_1 suppression could also be observed in the ternary PMHJ blends of D18/T9TBO-F:Y6-O and D18/T9SBN-F:Y6-O (Supplementary Figs. 43–45).

Considering different CS→T_1 relaxation pathways (Fig. 1a), the reduced signal intensity of T_1 in PMHJ may stem from (1) fewer polarons formed, which is contradictory to the higher J_{SC} observed from PMHJ devices (Supplementary Table 2); (2) low transfer efficiency of CS→^{1}CT/^{3}CT or ^{3}CT→T_1, which is more material-related thermodynamic properties and should be excluded since the material compositions used in this study are identical in the BHJ and PMHJ blends; and, most likely, (3) that the reduced D-A heterojunctions suppress the formation of recombined ^{1}CT/^{3}CT, therefore, hindering the back transfer pathways. To validate this hypothesis, the structural and morphological differences between BHJ and PMHJ blends were investigated by GIWAXS and resonant soft X-ray scattering (RSoXS; Supplementary Figs. 16–18 and Supplementary Tables 9–11). Both types of blends show similar GIWAXS profiles, including stacking distance, coherence length and molecular orientation. It should be noted that the best-performing D18/T9SBN-F exhibits the highest relative degree of ordering for (100), (010)
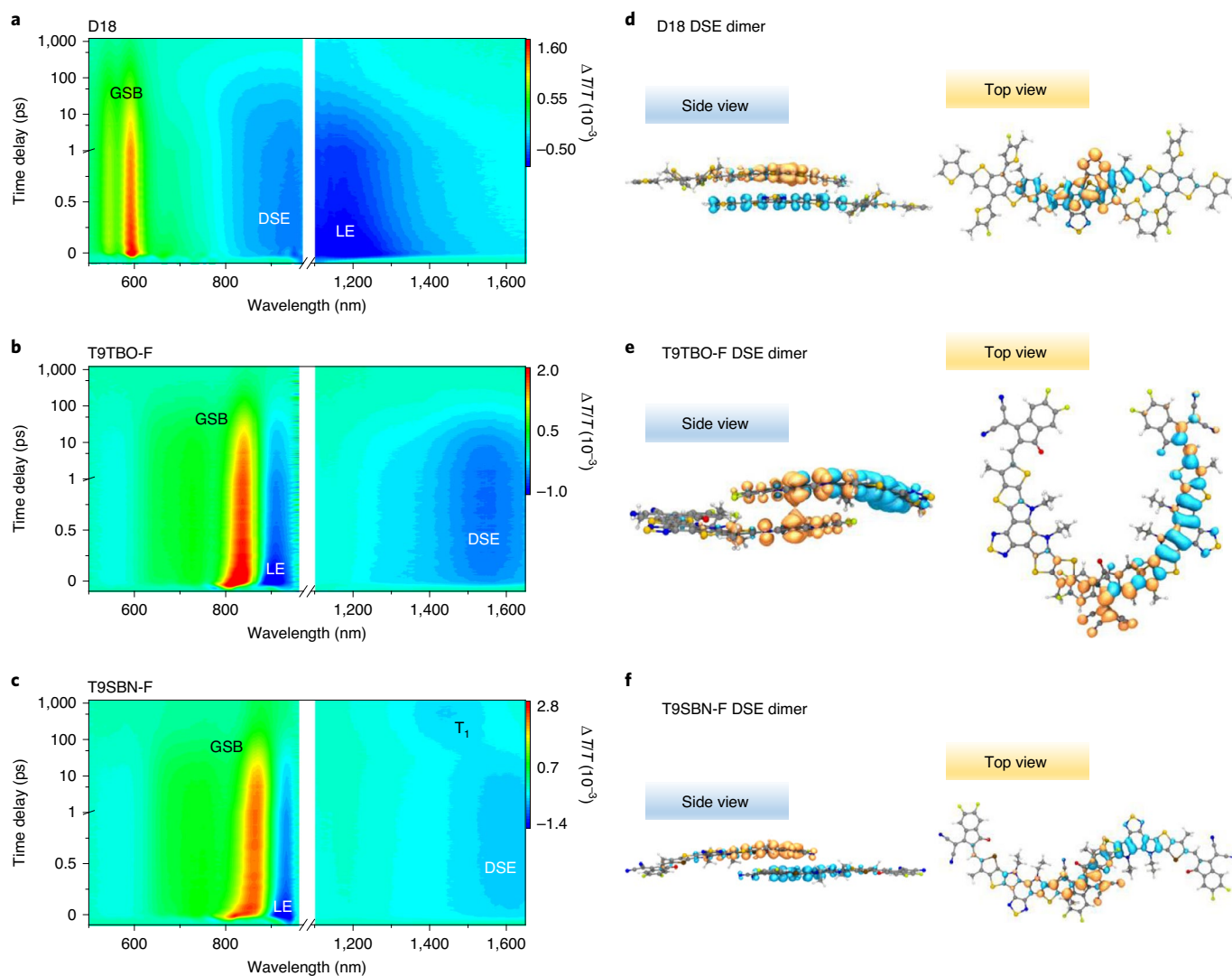
Fig. 3 | TA results and MD-simulated DSE dimers of neat materials. a–c, TA profiles for D18 (**a**), T9TBO-F (**b**) and T9SBN-F (**c**). The GSB/LE/DSE bands are 590/1,180/940 nm (D18); 825/915/1,550 nm (T9TBO-F); 840/930/1,600 nm (T9SBN-F). The intense ESA band at ~1,440 nm in T9SBN-F film matches the spectral feature of T_1 in NFAs identified by triplet sensitization, possibly

indicating efficient singlet–triplet intersystem crossing due to a heavy-atom effect (selenium). **d–f**, Representative packing patterns facilitating DSE formation in D18 (**d**), T9TBO-F (**e**) and T9SBN-F (**f**). Distribution of delocalized electrons and holes are in orange and blue, respectively.

and (002) peaks, as well as the highest face-on/edge-on ratio. The backbone peak (002) of D18 in PMHJ also exhibits a higher relative degree of ordering than that in BHJ, implying the distribution of more donor-rich phase in PMHJ (Supplementary Note IV). Importantly, RSoXS shows higher scattering intensity and, thus, higher in-plane composition variations in PMHJ, which can only arise due to some interpenetrations between the two layers. Moreover, following basic scattering theory and prior arguments[33,34], higher scattering intensity is corresponding to smaller numbers of D-A contacts from distributed A molecules in the mixed amorphous domains and the more discrete interfaces to D or A aggregates. Accordingly, a lower degree of molecular mixing as implied from the larger and purer domains is found in PMHJ than in BHJ (Supplementary Note V). Differences in composition gradients between BHJ and PMHJ were further confirmed with time-of-flight secondary ion mass spectrometry (ToF-SIMS) on D18/T9SBN-F, indicating some selenium enrichment towards the top of the PMHJ layer (Fig. 1e). Consequently, the non-geminately recombined $^1CT/^3CT$ states at D-A heterojunctions competing with charge extraction are depopulated, leading to less $^3CT \rightarrow T_1$ relaxation and improved J_{SC} in PMHJ cells. This

can be further supported by the higher normalized CS state intensity in the PMHJ samples than the BHJ ones, while normalizing the amplitude of CS state to that of LE in each of the corresponding samples (Supplementary Fig. 47).

Discussion
In addition to hindering the pathway mediating irreversible loss of photocarriers, it has been reported that suppressing T_1 formation could reduce non-radiative recombination to benefit V_{OC} in certain material systems where energetic inversion of ^1CT and ^3CT is possible due to the LE-CT hybridization[35]. However, a similar effect is not observed in the well-studied PM6:Y6 in which energetic inversion of ^1CT and ^3CT is absent[35]. Whereas in our PMHJ and BHJ cells, not only the V_{OC} values, but also the non-radiative V_{OC} losses are comparable (Fig. 2c–e, Supplementary Figs. 19, 20 and Supplementary Table 12). Therefore, the photovoltage and T_1 formation might not be directly correlated in our material systems containing Y6 derivatives. This finding provides an effective way to enhance J_{SC} without sacrificing V_{OC} in our PMHJ cells, while the non-radiative V_{OC} losses of ~0.24 eV in both D18/T9TBO-F and D18/
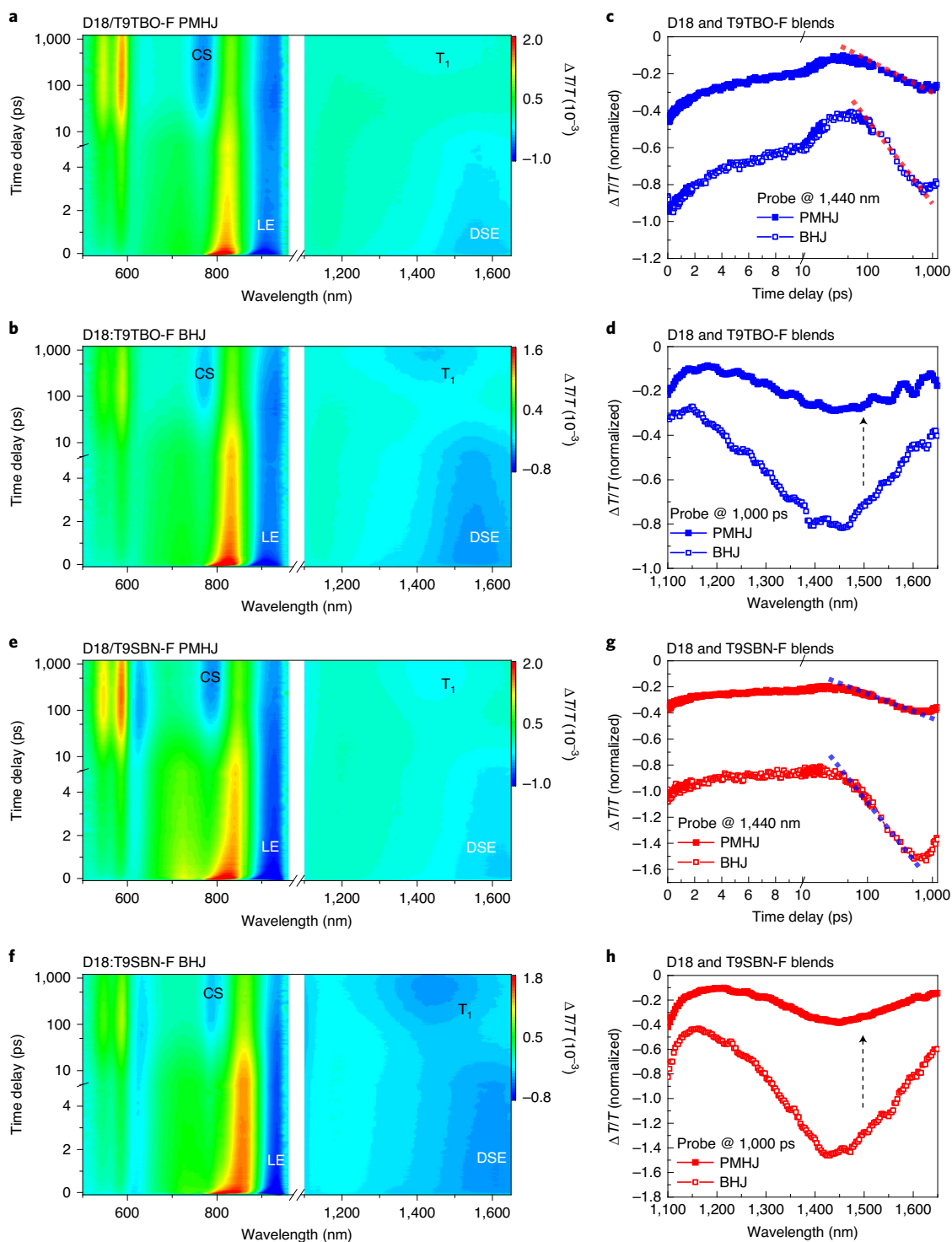
Fig. 4 | TA results of different blends. a,b,e,f, TA profiles of D18/T9TBO-F PMHJ (**a**) and D18:T9TBO-F BHJ (**b**), D18/T9SBN-F PMHJ (**e**) and D18:T9SBN-F BHJ (**f**). The GSB band of D18: 590 nm. The CS bands of blends: 765 nm (D18/T9TBO-F, D18:T9TBO-F); 790 nm (D18/T9SBN-F, D18:T9SBN-F). The T_1 signals of blends: -1,440 nm. **c,g,** The TA dynamics of ESA signals probed at 1,440 nm of D18/T9TBO-F and D18:T9TBO-F (**c**) and D18/T9SBN-F and D18:T9SBN-F (**g**). The slope dot lines were added to help guide the eyes. **d,h,** TA spectra probed at 1,000 ps time delay of D18/T9TBO-F and D18:T9TBO-F (**d**) and D18/T9SBN-F and D18:T9SBN-F (**h**). The arrow shows the trend of T_1 suppression in the PMHJ blend in comparison with the BHJ blend. All traces in **c, d, g** and **h** were respectively normalized to the minimum of corresponding CS bands in each sample.

T9SBN-F cells are comparable to those derived from high-efficiency narrow-bandgap organic absorbers[23–25].

In summary, we report a strategy to alleviate non-geminate recombination by depopulating the recombined CT states in sequentially deposited PMHJ OPVs with intrinsically reduced D-A heterojunctions, of which the suppressed T_1 formation can be observed as a signature. The efficient exciton dissociation in our PMHJ cells is ensured by employing photoactive materials with lower exciton binding strengths. High PCEs

surpassing 19% were subsequently achieved in OPVs with a PMHJ active layer based on the composites of polymer donor D18 and pseudo-2D Y6 NFA derivatives. The correlation between photocarrier generation efficiency and formation of recombined $^1CT/^3CT$ that affects J_{SC} in OPV is identified, consequently showing that a spin-mediated relaxation pathway causing irreversible energy loss is suppressed. The working mechanism lying in PMHJ has also been elucidated to provide a better understanding for improving OPV performance. Future efforts toward improving the stability of these PMHJ cells and uncovering the fundamental mechanisms of V_{OC} loss in these high-performance devices will further minimize the photovoltage–photocurrent trade-off, leading to PCEs greater than 20% to reach the theoretical limit of OPVs.

Methods

Materials

The synthesis of the unreported NFA structures is illustrated in Supplementary Scheme 1, with the detail regarding procedures and structural characterizations included in the Supplementary Information. Polymer donor D18 was synthesized according to the literature[12]. The full name of T9TBO-F is (2,10-bis(2-methylene-(3-(1,1-dicyanomethylene)-5,6-difluoroindanone))-12,13-bis(2-butyloctyl)-3,9-dinonyl-dithieno[2′,3′:4′,5′]thieno[2′,3′:4,5]pyrrolo[3,2-e:2′,3′-g][2,1,3]benzothiadiazole; the full name of T9SBN-F is (2,10-bis(2-methylene-(3-(1,1-dicyanomethylene)-5,6-difluoroindanone))-12,13-bis(3-butylnonyl)-3,9-dinonyl-diselenopheno[2′,3′:4′,5′]thieno[2′,3′:4,5]pyrrolo[3,2-e:2′,3′-g][2,1,3]benzothiadiazole. The full names of the rest of the synthesized NFAs are included in the Supplementary Information.

Material synthesis

Unless stated otherwise, all chemicals and reagents were used as received from commercial sources (Sigma-Aldrich, Acros, Matrix Scientific, Combi-Blocks, J&K Scientific, Energy) without further purification. Solvents for chemical synthesis were purified by distillation under nitrogen or by a solvent purification system (Innovative Technology, WellTech). All chemical reactions were carried out under an argon or nitrogen atmosphere. The ^{1}H and ^{13}C nuclear magnetic resonance spectra were recorded on a Bruker AV500, Bruker 400 MHz AVANCE III or a Bruker 600 MHz ASCEND AVANCE III HD spectrometer in CDCl$_3$ or d$_6$-DMSO. Mass spectrometry was performed on a Bruker APEX III 47e Fourier Transform mass spectrometer, or a Q Exactive Focus Hybrid Quadrupole Orbitrap Mass Spectrometer (QE Orbitrap MS, Thermo Fisher Scientific). The chemical structures and detailed synthetic procedure of the synthesized NFAs are included in the Supplementary Information.

Optical characteristics

UV-vis-NIR absorption spectra were recorded on a Shimadzu 1700 UV-vis spectrometer. The samples were spin-cast on quartz substrates and the thicknesses of films were measured by a Bruker Dektak XT stylus profilometer.

Energy level measurements

Ultraviolet photoelectron spectrometry (UPS) was performed to study the valence states of the materials with a He-discharge lamp providing He-I photos of 21.22 eV and a VG ESCALAB 220i-XL surface analyser. The absolute energy resolution of the analyser was set as 0.018 eV for the UPS measurement so that the spectral resolution was 0.09 eV as estimated from the Fermi edge of Au. During UPS measurement, a bias of −5.0 eV was applied to observe the lowest inelastic electrons kinetic energy cut-off. The bandgap (E_g) of the material was calculated from the optical absorption onset (λ_{onset}) of thin-film samples using the following equation: E_g (eV) = 1,240/λ_{onset}.

OPV cells

The OPV cells were fabricated with a conventional device architecture of glass/indium tin oxide (ITO)/poly(3,4-ethylenedioxythiophene):polystyrene sulfonate (PEDOT:PSS)/active layers/poly[(9,9-bis(3′-((N,N-dimethyl)-N-ethylammonium)propyl)-2,7-fluorene)-alt-5,5′-bis(2,2′-thiophene)-2,6-naphthalene-1,4,5,8-tetracarboxylic-N,N′-bis(2-ethylhexyl)imide] (PNDIT-F3N)/Ag. The ITO glass substrates (~15 Ω/sq) were cleaned with detergent (DECON 90), and then sequentially washed with deionized water, acetone and isopropanol in a sonication bath, each for 30 min. The cleaned ITO substrates were then dried in an oven overnight at 100 °C. Plasma treatment of 30 min was applied to ITO substrates prior to cell fabrication, after which PEDOT:PSS (Heraeus CLEVIOS™ P VP AI 4083) solution was spin-cast onto the ITO substrates at (5,000 r.p.m., 25 s), and then annealed at 120 °C for 15 min in ambient air.

Two-step processing of PMHJ (sequentially deposited D/A) cells

The slash in D/A stands for a sequentially processed film. The preparation of solutions and processing of thin films were carried out in a nitrogen-filled glove box with controlled environment (H$_2$O < 1 ppm, O$_2$ < 3 ppm, temperature = 25 ± 2 °C). Polymer donor (D18) solutions were prepared in chlorobenzene at a concentration of 6 mg ml^{-1}. Neat NIR-absorbing NFA solutions or their mixtures with Y6-O (10–20 wt%, Supplementary Table 3) were prepared in chloroform at a concentration of 10 mg ml^{-1}. To completely dissolve the materials, the D18 solution was stirred at 90 °C for at least 2 h and the NFA solution was stirred at 40 °C for 1 h. The D18 solutions were maintained at 90 °C during the whole fabrication procedure to avoid crush-out of polymer, while the NFA solutions were cooled to room temperature before use. The D18 layer was first dynamically spin-cast from its warm solution onto a pre-heated substrate (90 °C) at 3,000 r.p.m. (1,500 r.p.m. acceleration ramp) for 35 s to achieve a typical thickness of ~60 nm. Then an NFA layer was dynamically spin-cast from its solution on top of D18 layer at 2,000–2,200 r.p.m. (1,200 r.p.m. acceleration ramp) for 35 s to achieve an overall film thickness of ~110 nm, following with a thin layer of PNDIT-F3N (0.5-1 mg ml^{-1} in methanol at room temperature) dynamically spin-coated on top of the PMHJ active layer at 1,500 r.p.m. for 30 s (1,200 r.p.m. acceleration ramp). Finally, a layer of Ag (~110 nm) was thermally evaporated at 5 × 10^{-5} Pa through a shadow mask at a rate between 2.5–5 Å s^{-1}.

One-step processing of BHJ (mixed D:A) active layer

The colon in D:A stands for a film processed from a pre-mixed solution. The mixture of D18 and NFA (1:1.6 w/w) was dissolved in chloroform at a total concentration of 10 mg ml^{-1} and stirred at 50 °C overnight, then cooled to room temperature before use. The BHJ layer was processed by dynamically spin-coating onto a substrate at room temperature from its solution at 2,000–3,000 r.p.m. for 40 s (1,500 r.p.m. acceleration ramp), followed by chloroform solvent vapour annealing for 3 min in a petri dish (size: 60 mm × 15 mm) with 30 μl of chloroform.

J–V and EQE measurements

The thicknesses of films were measured by a Bruker Dektak XT stylus profilometer. The efficiencies of the cells were measured by a Keithley 2400 Source Meter under AM 1.5 G (100 mW cm^{-2}) irradiation using an EnliTech SS-F5 solar simulator. The light intensity was calibrated using a silicon solar cell (with a KG-2 filter) from the National Renewable Energy Laboratory. The cell area is defined by a metal mask with an aperture area of 4 mm^2 to ensure the accuracy of the current density obtained from the J–V measurements. EQE spectra were collected using an Enlitech QE-S EQE system equipped with a standard Si diode.

Single-crystal growth, ternary solvent diffusion

A solution prepared with ~1 mg NFA in 0.3 ml CHCl$_3$ was transferred into an NMR tube. On top of the CHCl$_3$ solution was carefully layered around 0.2 ml of CH$_2$Cl$_2$, followed by careful layering of acetone, using a glass pipet. The NMR tube was then sealed with parafilm and left standing undisturbed for 1–2 weeks until the colour of the solution faded away. The detailed information regarding the X-ray diffraction of single-crystals are included in the Supplementary Information.

GIWAXS measurements

GIWAXS measurements were performed at beamline 7.3.3[36] at the Advanced Light Source. Samples were prepared on Si substrates using optimized conditions for OPV fabrication. The incident angle of the 10 keV X-ray beam was set at 0.13° to maximize the scattering intensity from the samples. The scattered X-rays were detected using a Dectris Pilatus 1-M photon-counting detector. All measurements were conducted under a helium atmosphere to reduce air scattering. In-plane and out-of-plane sector averages were calculated using the Nika software package. The coherence length was calculated using the Scherrer equation: $CL = 2\pi K/\Delta q$, where Δq is the full-width at half-maximum of the peak and K is a shape factor (1 was used in this work).

RSoXS measurements

RSoXS transmission measurements were performed at beamline 11.0.1.2[37] at the Advanced Light Source. Samples for RSoXS measurement were prepared on PSS-coated Si substrates using optimized conditions for OPV fabrication, and then transferred by floating in deionized water to a 1.5 mm × 1.5 mm, 100 nm thick Si_3N_4 membrane supported by a 5 mm × 5 mm, 200 μm thick Si frame (Norcada). Two-dimensional scattering patterns were collected on an in-vacuum CCD camera. The in-plane composition variation (related to the relative domain purity) over the length scales probed can be extracted by integrating scattering profiles to yield the integrated scattering intensity (ISI). The purer the average domains are, the higher the ISI. Owing to a lack of absolute flux normalization, the absolute composition cannot be obtained only by RSoXS.

ToF-SIMS

ToF-SIMS measurement was performed using a TOF-SIMS V instrument (ION-TOF GmbH, Cameca IMS 4 F), where a 3 keV Cs⁺ ion beam was used for erosion and a 25 keV Bi³⁺ pulsed primary ion beam was used for the analysis. The area of analysis was 50 × 50 μm² while the sputtering area was 300 × 300 μm². The measurement was performed on the D18/T9SBN-F PMHJ blend and D18:T9SBN-F BHJ blend, in which the distribution of T9SBN-F was tracked using Se^{2-} ion as the characteristic species.

MD calculation

MD force field parameter optimization. The MD simulation was performed on different types of D18-NFA blends to mimic different degree of D-A mixing, including blends in bilayer (BL) and BHJ forms. The BL blend was used as a simplified model of PMHJ, which possesses less D-A interfaces and higher domain purity. The BL film was first constructed by a layer of D18, followed by constructing another layer of NFA molecules on top. The BHJ film was constructed by randomly dispersing D18 and NFA molecules in a confined space.

The MD simulation was performed in the Gromacs 2021 package[38]. The GAFF2 force field was used as initial parameters. The equilibrium bond lengths and angles were updated based on optimized geometries. The atomic partial charges were calculated at the PBE0/def2-SVP level of theory, and fitted using the restrained electrostatic potential (RESP) method by Multiwfn. The dihedral potentials that dictate the planarity of the conjugated molecules were fitted to the PBE0-D3BJ/def2-SVP potential energy surfaces. For MD simulation of D18:T9SBN-F, the Lennard-Jones parameters of element Se in T9SBN-F were calculated by methods described previously[39]. The force constants of bonds and angles containing Se were calculated by modified Seminario method[40]. The obtained ε and σ for Se are 1.26 kJ mol⁻¹ and 0.364 nm, respectively.

MD system construction and simulation

For all systems, 900 NFA molecules and 150 segments of D18 hexamers were used for the simulation, to give a 1:1 molar ratio between D18 repeating units and NFAs.

The bilayer (BL) blends were constructed using the following procedure. First, the D18 hexaamers were randomly placed into a rectangle box with edge lengths of 15 × 15 × 150 nm using packmol software[41]. Two VDW walls were placed at $z = 0$ nm and $z = z_{max}$ for the following simulations. The isothermal-isobaric ensemble (NPT) run was performed for 20 ns with five annealing cycles between 500 K and 300 K. During the annealing, semi-isotropic Berendsen barostat with pressure and compressibility of xy was set to zero to compress the system in z direction. A vacuum slab of 20 nm was built on top of the compressed D18 film, followed by a minimization and a canonical ensemble (NVT) run at 300 K to relax the surface. The NFA molecules were then added loosely on top of the slab with $z_{max} = 150$ nm. Another annealing NPT run was performed with similar condition to compress the NFA layer. The system was then equilibrated at 300 K NPT for 10 ns. Finally, the production NPT run was performed at 300 K for 10 ns to obtain the trajectories.

The BHJ blends were constructed using the following procedure. First, the molecules were randomly placed into a cubic box with an edge length of 40 nm using packmol software[41]. Then, the NPT run was performed for 20 ns with five annealing cycles between 500 K and 300 K to compress the structures. The system was further equilibrated at 300 K for a 10 ns NPT run. Lastly, the production NPT run was performed at 300 K for 10 ns to obtain the trajectories.

All of the MD simulations were employed with velocity-Verlet integrator at 2.0 fs time step with LINCS algorithm to constrain bonds with hydrogen. The temperature was controlled with V-rescale thermostat[42]. The pressure was controlled using Berendsen barostat. Three independent simulations were performed for each system. And the analysis was performed on the frames extracted from the 10 ns production run with 200 ps interval.

Neighbour atom analysis

The D18 donor is divided into D_A (electron-accepting moiety), D_D (electron-donating moiety), D_π (π-bridge) fragments, and the NFA is divided into A_A (electron-accepting moiety), A_D (electron-donating moiety) fragments as shown in Supplementary Fig. 3. Heavy atoms within a distance of 3.6 Å to each other, and hydrogen atoms within a distance of 3 Å to heavy atoms, are defined as 'neighbour atoms' for all fragments. The count of neighbour atoms was then summed over all the 150 frames from three trajectories followed by classification according to correlating fragments. The analysis was performed using MDAnalysis package[43].

Density functional theory calculation

For isolated D18 dimer, T9TBO-F and T9SBN-F, all the alkyl chains were replaced with ethyl groups. The ground-state (S_0) geometries were optimized at PBE0/def2-SVP level with Grimme's D3 dispersion correction with BJ dampening[44]. The excited-state (LE) geometries of D18 monomer, T9TBO-F and T9SBN-F are optimized at TD-PBE0-D3BJ/def2-SVP level followed by ω-tuned TD-LC-wHPBE/def2-SVP[45] calculations to obtain electronic structure of LE state. Electron-hole analysis was performed using Multiwfn v.3.8[46] to obtain electron-hole overlap and visualize exciton delocalization. SMD solvation model[47] was used for all the calculations using diphenylether ($\varepsilon = 3.73$) as a solvent to imitate the dielectric environment in solids. For the formation of DSE, the molecular pairs of D18 monomer and NFAs were constructed by extracting close contact pairs from MD simulations of blend films. The electronic structure of S_1 state of these molecular pairs were obtained following the same procedures as that of isolated molecules. All the density functional theory calculations were carried out using Gaussian 16 program[48].

TA measurements

The fs-TA measurements were conducted using a Yb:KGW laser (Pharos, Light Conversion). The wavelength of fundamental output was at -1,030 nm. We used a home-built noncollinear optical parametric amplifier to generate the pump pulses at 800 nm, 900 nm and 610 nm,

respectively. The probe beam was supercontinuum by focusing a small fraction of the fundamental 1030 beam to a 5 mm sapphire plate for visible detection or a 6 mm yttrium aluminium garnet (YAG) plate for infrared detection. A short pass filter (10SWF-1000-B, Newport) or a long pass filter (FELH1100, Thorlabs) was employed in the supercontinuum to exclude the fundamental beam for visible detection (550–950 nm) or infrared detection (1,100–1,600 nm), respectively. The pump and visible probe pulses were compressed by chirp mirrors and wedge pairs to maintain a time resolution better than 40 fs. The supercontinuum light was split into two beams for balanced detection. The probe and reference beams were then routed to either a double-line Si camera (S14417, Hamamatsu) for visible detection or a double-line InGaAs camera (G11608, Hamamatsu) for infrared detection. The cameras were mounted on a monochromator (Acton 2358, Princeton Instrument). Pulse-to-pulse spectral analysis was conducted at 50 kHz for visible detection and 16 kHz for infrared detection using a homemade field-programmable gate array (FPGA) control board. The signal-to-noise ratio ($\Delta T/T$) was better than 1×10^{-5} after averaging 25,000 pump-on and pump-off shots for each data point. In the ns-TA measurements, the pump laser was replaced by a pulsed laser diode emitted at 670 nm (LDH-P-C-670M, Picoquant). The time delay between the two lasers was synchronized and enabled by a digital delay generator (DG645, Stanford Research System). The pump fluence was set at 2 μJ cm^{-2} unless otherwise specified. The samples were kept in a nitrogen atmosphere during the measurement to prevent photo-degradation.

Photo-induced absorption measurements

The photo-induced absorption (PIA) measurements were also conducted using the Yb:KGW laser (Pharos, Light Conversion). In the PIA measurements, the pump light was replaced with a cw laser (MW-ZIR-808) at 800 nm modulated at 2.5 kHz by a chopper. The pump fluence was set at 60 mW cm^{-2} at the same level of pump density of AM 1.5 G in the visible range. The probe light was set 180 μs after the pump light to obtain the PIA signals. For the probe range of 950–1,100 nm, the probe light was generated by focusing the output beam at 1,500 nm from a homemade OPA onto a 5-mm sapphire plate.

Triplet sensitization of NFAs

For the solution samples, we mixed the NFA with an appropriate amount of platinum octaethylporphyrin (PtOEP, Sigma-Aldrich) triplet sensitizer (total concentration, 0.5 mg ml^{-1}, PtOEP:NFA = 3:1 w/w) in a quartz cuvette to ensure sufficient energy transfer from PtOEP to NFA molecules in the rather diluted environment. The sample was pumped at 355 nm (third harmonic generation of 1,064 nm, picolo 50, INNOLAS Germany). The time delay between the pump and probe lasers was synchronized and enabled by a digital delay generator (DG645, Stanford Research System). The film samples were prepared by coating a solution containing NFA and PtOEP (total concentration, 10 mg ml^{-1}; PtOEP:NFA = 1:3 w/w) onto the substrates. The TA measurements were conducted employing a Ti:sapphire regenerative amplifier (Libra, Coherent) at ~800 nm with a repetition rate of 1 kHz and pulse duration of 90 fs. An optical parametric amplifier (OperA Solo, Coherent) pumped by the regenerative amplifier was used to generate the pump beam at 385 nm. The probe beam of supercontinuum in the infrared wavelength range were generated by focusing a small portion of the femtosecond laser beam onto a 1-cm thick sapphire plate. A long pass filter (FGL850, Thorlabs) was employed in the supercontinuum to exclude the fundamental beam for infrared detection (900–1,600 nm). The supercontinuum light was split into two beams for balanced detection. The probe and reference beams were then routed to a homemade double-line InGaAs camera (G11608, Hamamatsu) for infrared detection. The camera was mounted on a monochromator (Acton 2358, Princeton Instrument). The signal-to-noise ratio reaches 1×10^{-4} after averaging 1,000 couples of pump-on and pump-off spectra. The pump

fluence was set at about 2 μJ cm^{-2}. The samples were kept in a nitrogen atmosphere during the measurement.

Reporting summary

Further information on research design is available in the Nature Research Reporting Summary linked to this article.

Data availability

The authors declare all data supporting the findings of this study are available within the manuscript and the Supplementary Information. The .cif files corresponding to single-crystal structures reported in this work are available from Cambridge Crystallographic Data Centre (T9TBO-F: 2081901; T9SBN-F: 2084244 and 2081902). The source data of Supplementary Table 2 and Supplementary Fig. 6c,d are provided as Supplementary Data 1 and 2.

References

1. Yan, C. et al. Non-fullerene acceptors for organic solar cells. *Nat. Rev. Mater.* **3**, 18003 (2018).
2. Yuan, J. et al. Single-junction organic solar cell with over 15% efficiency using fused-ring acceptor with electron-deficient core. *Joule* **3**, 1140–1151 (2019).
3. Lin, Y. et al. An electron acceptor challenging fullerenes for efficient polymer solar cells. *Adv. Mater.* **27**, 1170–1174 (2015).
4. Tang, C. W. Two-layer organic photovoltaic cell. *Appl. Phys. Lett.* **48**, 183–185 (1986).
5. Yu, G., Gao, J., Hummelen, J. C., Wudl, F. & Heeger, A. J. Polymer photovoltaic cells: enhanced efficiencies via a network of internal donor-acceptor heterojunctions. *Science* **270**, 1789–1791 (1995).
6. Cha, H. et al. Exciton and charge carrier dynamics in highly crystalline PTQ10:IDIC organic solar cells. *Adv. Energy Mater.* **10**, 2001149 (2020).
7. Jiang, K. et al. Pseudo-bilayer architecture enables high-performance organic solar cells with enhanced exciton diffusion length. *Nat. Commun.* **12**, 468 (2021).
8. Hou, J., Inganäs, O., Friend, R. H. & Gao, F. Organic solar cells based on non-fullerene acceptors. *Nat. Mater.* **17**, 119–128 (2018).
9. Zhu, L., Yi, Y. & Wei, Z. Exciton binding energies of nonfullerene small molecule acceptors: implication for exciton dissociation driving forces in organic solar cells. *J. Phys. Chem. C* **122**, 22309–22316 (2018).
10. Zhang, G. et al. Delocalization of exciton and electron wavefunction in non-fullerene acceptor molecules enables efficient organic solar cells. *Nat. Commun.* **11**, 3943 (2020).
11. Lin, F., Jiang, K., Kaminsky, W., Zhu, Z. & Jen, A. K. Y. A non-fullerene acceptor with enhanced intermolecular π-core interaction for high-performance organic solar cells. *J. Am. Chem. Soc.* **142**, 15246–15251 (2020).
12. Liu, Q. et al. 18% Efficiency organic solar cells. *Sci. Bull.* **65**, 272–275 (2020).
13. Rao, A. et al. The role of spin in the kinetic control of recombination in organic photovoltaics. *Nature* **500**, 435–439 (2013).
14. Schlenker, C. W. et al. Polymer triplet energy levels need not limit photocurrent collection in organic solar cells. *J. Am. Chem. Soc.* **134**, 19661–19668 (2012).
15. Qin, L. et al. Triplet acceptors with a D-A structure and twisted conformation for efficient organic solar cells. *Angew. Chem. Int. Ed.* **59**, 15043–15049 (2020).
16. Wang, R. et al. Nonradiative triplet loss suppressed in organic photovoltaic blends with fluoridated nonfullerene acceptors. *J. Am. Chem. Soc.* **143**, 4359–4366 (2021).
17. Chen, Z. et al. Triplet exciton formation for non-radiative voltage loss in high-efficiency nonfullerene organic solar cells. *Joule* **5**, 1832–1844 (2021).

18. Wang, R. et al. Charge separation from an intra-moiety intermediate state in the high-performance PM6:Y6 organic photovoltaic blend. *J. Am. Chem. Soc.* **142**, 12751–12759 (2020).

19. Sun, R. et al. A layer-by-layer architecture for printable organic solar cells overcoming the scaling lag of module efficiency. *Joule* **4**, 407–419 (2020).

20. Weng, K. et al. Optimized active layer morphology toward efficient and polymer batch insensitive organic solar cells. *Nat. Commun.* **11**, 2855 (2020).

21. Ye, L. et al. Sequential deposition of organic films with eco-compatible solvents improves performance and enables over 12%-efficiency nonfullerene solar cells. *Adv. Mater.* **31**, 1808153 (2019).

22. Wang, Z. et al. Thermodynamic properties and molecular packing explain performance and processing procedures of three D18:NFA organic solar cells. *Adv. Mater.* **32**, 2005386 (2020).

23. Zhang, Z. et al. Selenium heterocyclic electron acceptor with small urbach energy for as-cast high-performance organic solar cells. *J. Am. Chem. Soc.* **142**, 18741–18745 (2020).

24. Liu, S. et al. High-efficiency organic solar cells with low non-radiative recombination loss and low energetic disorder. *Nat. Photonics* **14**, 300–305 (2020).

25. Qian, D. et al. Design rules for minimizing voltage losses in high-efficiency organic solar cells. *Nat. Mater.* **17**, 703–709 (2018).

26. Armin, A. et al. A history and perspective of non-fullerene electron acceptors for organic solar cells. *Adv. Energy Mater.* **11**, 2003570 (2021).

27. Jiang, K. et al. Alkyl chain tuning of small molecule acceptors for efficient organic solar cells. *Joule* **3**, 3020–3033 (2019).

28. Cui, Y. et al. Single-junction organic photovoltaic cells with approaching 18% efficiency. *Adv. Mater.* **32**, 1908205 (2020).

29. Chen, Y. et al. Alkoxy substitution on IDT-Series and Y-Series non-fullerene acceptors yielding highly efficient organic solar cells. *J. Mater. Chem. A* **9**, 7481–7490 (2021).

30. Chen, H. et al. 17.6%-efficient quasiplanar heterojunction organic solar cells from a chlorinated 3D network acceptor. *Adv. Mater.* **33**, 2102778 (2021).

31. Firdaus, Y. et al. Long-range exciton diffusion in molecular non-fullerene acceptors. *Nat. Commun.* **11**, 5220 (2020).

32. Yang, L. et al. Triplet tellurophene-based acceptors for organic solar cells. *Angew. Chem. Int. Ed.* **57**, 1096–1102 (2018).

33. Karki, A. et al. Unifying charge generation, recombination, and extraction in low-offset non-fullerene acceptor organic solar cells. *Adv. Energy Mater.* **10**, 2001203 (2020).

34. Ye, L. et al. Quantitative relations between interaction parameter, miscibility and function in organic solar cells. *Nat. Mater.* **17**, 253–260 (2018).

35. Gillett, A. J. et al. The role of charge recombination to triplet excitons in organic solar cells. *Nature* **597**, 666–671 (2021).

36. Hexemer, A. et al. A SAXS/WAXS/GISAXS beamline with multilayer monochromator. *J. Phys. Conf. Ser.* **247**, 012007 (2010).

37. Gann, E. et al. Soft x-ray scattering facility at the Advanced Light Source with real-time data processing and analysis. *Rev. Sci. Instrum.* **83**, 045110 (2012).

38. Abraham, M. J. et al. GROMACS: High performance molecular simulations through multi-level parallelism from laptops to supercomputers. *SoftwareX* **1-2**, 19–25 (2015).

39. Cole, D. J., Vilseck, J. Z., Tirado-Rives, J., Payne, M. C. & Jorgensen, W. L. Biomolecular force field parameterization via atoms-in-molecule electron density partitioning. *J. Chem. Theory Comput.* **12**, 2312–2323 (2016).

40. Allen, A. E. A., Payne, M. C. & Cole, D. J. Harmonic force constants for molecular mechanics force fields via hessian matrix projection. *J. Chem. Theory Comput.* **14**, 274–281 (2018).

41. Martínez, L., Andrade, R., Birgin, E. G. & Martínez, J. M. PACKMOL: A package for building initial configurations for molecular dynamics simulations. *J. Comput. Chem.* **30**, 2157–2164 (2009).

42. Bussi, G., Donadio, D. & Parrinello, M. Canonical sampling through velocity rescaling. *J. Chem. Phys.* **126**, 014101 (2007).

43. Michaud-Agrawal, N., Denning, E. J., Woolf, T. B. & Beckstein, O. MDAnalysis: A toolkit for the analysis of molecular dynamics simulations. *J. Comput. Chem.* **32**, 2319–2327 (2011).

44. Grimme, S., Ehrlich, S. & Goerigk, L. Effect of the damping function in dispersion corrected density functional theory. *J. Comput. Chem.* **32**, 1456–1465 (2011).

45. Henderson, T. M., Izmaylov, A. F., Scalmani, G. & Scuseria, G. E. Can short-range hybrids describe long-range-dependent properties? *J. Chem. Phys.* **131**, 044108 (2009).

46. Lu, T. & Chen, F. Multiwfn: A multifunctional wavefunction analyzer. *J. Comput. Chem.* **33**, 580–592 (2012).

47. Marenich, A. V., Cramer, C. J. & Truhlar, D. G. Universal solvation model based on solute electron density and on a continuum model of the solvent defined by the bulk dielectric constant and atomic surface tensions. *J. Phys. Chem. B* **113**, 6378–6396 (2009).

48. Frisch, M. J. et al. Gaussian 16 Rev. C.01 (2016).

49. Rau, U. Reciprocity relation between photovoltaic quantum efficiency and electroluminescent emission of solar cells. *Phys. Rev. B* **76**, 085303 (2007).

50. Ziffer, M. E. et al. Long-lived, non-geminate, radiative recombination of photogenerated charges in a polymer/small-molecule acceptor photovoltaic blend. *J. Am. Chem. Soc.* **140**, 9996–10008 (2018).

Acknowledgements

Author contributions

K.J., F.R.L., J.Z., C. Zhang and A.K.-Y.J. conceived the project. K.J., F.R.L. and J.Z. designed the experiments. K.J. fabricated and characterized the cells. F.R.L. and F.Q. synthesized the materials and grew the single crystals. J.Z., Q.L., M.X. and C. Zhang conducted TA experiments and corresponding analysis. C. Zhong conducted the MD, density functional theory and Marcus rate calculations. W.K. solved the single-crystal structures. S.H.J. and F.R.L. analysed the molecular

Competing interests

The authors declare no competing interests.

Additional information

Supplementary information The online version contains supplementary material available at
https://doi.org/10.1038/s41560-022-01138-y.

Correspondence and requests for materials should be addressed to Francis R. Lin, Chunfeng Zhang or Alex K.-Y. Jen.

Peer review information *Nature Energy* thanks Peter Müller-Buschbaum and the other, anonymous, reviewer(s) for their contribution to the peer review of this work.

Reprints and permissions information is available at www.nature.com/reprints.

nature research

Corresponding author(s):   Alex K.-Y. Jen, Chunfeng Zhang, Francis R. Lin

Solar Cells Reporting Summary

Nature Research wishes to improve the reproducibility of the work that we publish. This form is intended for publication with all accepted papers reporting the characterization of photovoltaic devices and provides structure for consistency and transparency in reporting. Some list items might not apply to an individual manuscript, but all fields must be completed for clarity.

For further information on Nature Research policies, including our data availability policy, see Authors & Referees.

▶ Experimental design

Please check: are the following details reported in the manuscript?

1. Dimensions

   Area of the tested solar cells
   ☒ Yes ☐ No
   In our lab, the area of the solar cells tested is 4 mm2 (Methods section: J-V and EQE measurements).

   Method used to determine the device area
   ☒ Yes ☐ No
   In our lab, the area of the solar cells tested is defined by a non-reflective metal mask with an aperture area of 4 mm2 (Methods section: J-V and EQE measurements).

2. Current-voltage characterization

   Current density-voltage (J-V) plots in both forward and backward direction
   ☒ Yes ☐ No
   For the cell sent to Newport Co. for certification, forward and backward scans were performed on the cell before the asymptotic scans (Supplementary Figure 7).
   For the cell sent to IEE, Chinese Academy of Sciences for certification, a single reverse scan was performed (Supplementary Figure 9).
   For the cells tested in our lab, as hysteresis is generally negligible in OPV cells, a single forward scan was conducted to determine their J-V profiles.

   Voltage scan conditions
   For instance: scan direction, speed, dwell times
   ☒ Yes ☐ No
   For the cells tested in our lab, the scan was performed in the range from -0.2 to 1.0 or 1.2 V, with a scan step of 0.02 V and dwell time of 10 ms.
   The voltage scan conditions during certifications were provided in Supplementary Figures 7 and 9.

   Test environment
   For instance: characterization temperature, in air or in glove box
   ☒ Yes ☐ No
   For the cells tested in our lab, the cells were non-encapsulated and the measurements were performed in an N2-filled glove box at room temperature.
   For the cells sent to certifications, the cells were encapsulated and the measurements were carried out in ambient atmosphere at room temperature.
   Further details regarding test environment during certifications were provided in Supplementary Figures 7 and 9.

   Protocol for preconditioning of the device before its characterization
   ☒ Yes ☐ No
   For the cell sent to Newport Co. for certification, several J-V sweeps were conducted before the asymptotic scans, which were use to determine the certified cell performance (Supplementary Figure 7).
   For the cells tested in our lab, no preconditioning was applied.

   Stability of the J-V characteristic
   Verified with time evolution of the maximum power point or with the photocurrent at maximum power point; see ref. 7 for details.
   ☒ Yes ☐ No
   For the cell sent to Newport Co. for certification, the stability of J-V characteristics were confirmed by asymptotic scans (Supplementary Figure 7).

3. Hysteresis or any other unusual behaviour

   Description of the unusual behaviour observed during the characterization
   ☐ Yes ☒ No
   There is no unusual behavior observed during the characterization, i.e, hysteresis.

   Related experimental data
   ☐ Yes ☒ No
   We are not reporting unusual behavior.

4. Efficiency

   External quantum efficiency (EQE) or incident photons to current efficiency (IPCE)
   ☒ Yes ☐ No
   The EQE spectra were collected using an Enlitech QE-S EQE system equipped with a standard Si diode, as shown in Figure 2b.

   A comparison between the integrated response under the standard reference spectrum and the response measure under the simulator
   ☒ Yes ☐ No
   The values of the integrated current from EQE and the short-circuit current from J-V curve measured under AM 1.5G solar simulator are within 4% difference, which is within the accuracy confidence of the measurements.

For tandem solar cells, the bias illumination and bias voltage used for each subcell	☐ Yes ☒ No	We do not report tandem solar cells in this work.

5. Calibration

Light source and reference cell or sensor used for the characterization	☒ Yes ☐ No	In our lab, the cells were measured under AM 1.5G (100 mW cm-2) irradiation using an EnliTech SS-F5 solar simulator. The light intensity was calibrated using a silicon solar cell (with a KG-2 filter) from the National Renewable Energy Laboratory (Methods section: J-V and EQE measurements). For the cells sent to certifications, please refer to Supplementary Figure 7 (Newport Co.) and Supplementary Figure 9 (IEE, Chinese Academy of Sciences).
Confirmation that the reference cell was calibrated and certified	☒ Yes ☐ No	The solar simulator in our lab is equipped with a silicon solar cell (with a KG-2 filter) from the National Renewable Energy Laboratory (Methods section: J-V and EQE measurements). For the cells sent to certifications, calibrated and certified reference cells were used (Supplementary Figures 7 and 9).
Calculation of spectral mismatch between the reference cell and the devices under test	☒ Yes ☐ No	In our lab, the spectral mismatch between the reference cell and the tested devices is calculated to be around 1 with a deviation < 1%. For the cell sent to Newport Co. for certification, the spectral mismatch was calculated as M=1.013 +/- 0.015. (Supplementary Figure 7)

6. Mask/aperture

Size of the mask/aperture used during testing	☒ Yes ☐ No	For the cells tested in our lab, the mask/aperture area is 4 mm2. (Methods section: J-V and EQE measurements). For the cells sent to certifications, the aperture area was defined as 3.965 +/- 0.029 mm2 (Newport Co., Supplementary Figure 7) and 3.713 mm2 (IEE, Chinese Academy of Sciences, Supplementary Figure 9).
Variation of the measured short-circuit current density with the mask/aperture area	☐ Yes ☒ No	For the cells tested in our lab, all cells were measured using one identical mask.

7. Performance certification

Identity of the independent certification laboratory that confirmed the photovoltaic performance	☒ Yes ☐ No	Two cells were respectively certified by Newport Co. (asymptotic scans, Supplementary Figure 7) and Photovoltaic and Wind Power Systems Quality Test Center, IEE, Chinese Academy of Sciences (J-V sweep, Supplementary Figure 7).
A copy of any certificate(s) *Provide in Supplementary Information*	☒ Yes ☐ No	The copy of certificates are provided as Supplementary Figure 7 (Newport Co.) and 9 (Photovoltaic and Wind Power Systems Quality Test Center, IEE, Chinese Academy of Sciences).

8. Statistics

Number of solar cells tested	☒ Yes ☐ No	The information is provided in Supplementary Table 2 and Supplementary Figure 6.
Statistical analysis of the device performance	☒ Yes ☐ No	The information is provided in Supplementary Table 2 and Supplementary Figure 6.

9. Long-term stability analysis

Type of analysis, bias conditions and environmental conditions *For instance: illumination type, temperature, atmosphere humidity, encapsulation method, preconditioning temperature*	☐ Yes ☒ No	The long-term stability of the cells is not the main focus of this work, however we understand this is a critical topic in the field and we are currently working on it too.